Stability of exomoons around the *Kepler* transiting circumbinary planets

Adrian S. Hamers[1]⋆, Maxwell X. Cai[2]†, Javier Roa[3]‡, and Nathan Leigh[4,5]§
[1]*Institute for Advanced Study, School of Natural Sciences, Einstein Drive, Princeton, NJ 08540, USA*
[2]*Leiden Observatory, Leiden University, PO Box 9513, NL-2300 RA Leiden, The Netherlands*
[3]*Jet Propulsion Laboratory, California Institute of Technology, 4800 Oak Grove Dr, Pasadena, CA 91109, USA*
[4]*Department of Astrophysics, American Museum of Natural History, Central Park West and 79th Street, New York, NY 10024, USA*
[5]*Department of Physics and Astronomy, Stony Brook University, Stony Brook, NY 11794-3800, USA*

ABSTRACT

The *Kepler* mission has detected a number of transiting circumbinary planets (CBPs). Although currently not detected, exomoons could be orbiting some of these CBPs, and they might be suitable for harboring life. A necessary condition for the existence of such exomoons is their long-term dynamical stability. Here, we investigate the stability of exomoons around the *Kepler* CBPs using numerical N-body integrations. We determine regions of stability and obtain stability maps in the $(a_\mathrm{m}, i_\mathrm{pm})$ plane, where a_m is the initial exolunar semimajor axis with respect to the CBP, and i_pm is the initial inclination of the orbit of the exomoon around the planet with respect to the orbit of the planet around the stellar binary. Ignoring any dependence on i_pm, for most *Kepler* CBPs the stability regions are well described by the location of the 1:1 mean motion resonance (MMR) of the binary orbit with the orbit of the moon around the CBP. This can be ascribed to a destabilizing effect of the binary compared to the case if the binary were replaced by a single body, and which is borne out by corresponding 3-body integrations. For high inclinations, the evolution is dominated by Lidov-Kozai oscillations, which can bring moons in dynamically stable orbits to close proximity within the CBP, triggering strong interactions such as tidal evolution, tidal disruption, or direct collisions. This suggests that there is a dearth of highly-inclined exomoons around the *Kepler* CBPs, whereas coplanar exomoons are dynamically allowed.

Key words: gravitation – planets and satellites: dynamical evolution and stability – planet-star interactions

1 INTRODUCTION

One of the exotic type of planetary systems detected by the *Kepler* mission are transiting circumbinary planets (CBPs), i.e., planets in nearly-coplanar orbits around a stellar binary (and nearly coplanar with the plane of the sky), temporarily blocking the binary's light and giving a generally complex light curve (e.g., Martin & Triaud 2015; Martin 2017). Currently, 10 confirmed *Kepler* CBPs are known in 9 binary systems (see Table 1 for an overview). These systems have revealed important clues for the formation and evolution of planets and high-order multiple systems. For example, none of the *Kepler* CBPs are orbiting binaries with periods shorter than 7 d, which suggests the presence of a third star (Muñoz & Lai 2015; Martin et al. 2015; Hamers et al. 2016), or could be indicative of coupled stellar-tidal evolution (Fleming et al. 2018).

A key question for the CBP systems is whether they would be able to harbour life. As shown by various authors (Orosz et al. 2012a; Quarles et al. 2012; Kane & Hinkel 2013; Haghighipour & Kaltenegger 2013; Cuntz 2014, 2015; Zuluaga et al. 2016; Wang & Cuntz 2017; Moorman et al. 2018), some of the *Kepler* CBPs are within the habitable zone (HZ). Some of the *Kepler* CBPs are giant planets and are unlikely to be able to sustain life; on the other hand, exomoons are prime candidates for celestial objects harbouring life (e.g., Lammer et al. 2014; Sato et al. 2017; Dobos et al. 2017). Although techniques to observe exomoons have been developed, they have not yet been found (e.g., Kipping 2009a,b; Kipping et al. 2012, 2013a,b, 2014; see Kipping 2014 for a review). Given the abundance of moons in the Solar system, it is reasonable to assume that they exist.

A necessary condition for the existence of exomoons in the *Kepler* CBPs is that they be long-term dynamically stable. In this paper, we address this issue by carrying out N-body integrations of exomoons orbiting around the *Kepler* CBPs (i.e., in S-type orbits around the CBPs, Dvorak 1984). We will show that stable configurations are possible for a wide range of parameters, and that the sta-

---

⋆ E-mail: hamers@ias.edu
† cai@strw.leidenuniv.nl
‡ javier.roa@jpl.nasa.gov
§ nleigh@amnh.org

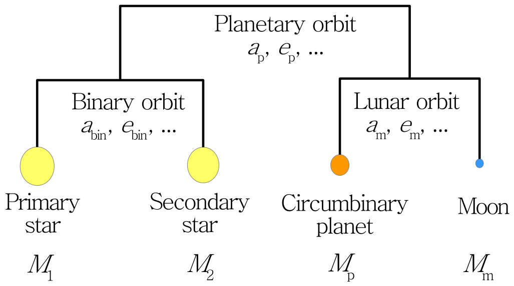

Figure 1. Schematic representation (not to scale) of the orbits of the stellar binary, the CBP, and its moon.

bility boundary is mediated by mean motion resonances (MMRs) with the stellar binary.

We note a previous work by Quarles et al. (2012), who considered the dynamical stability (and habitability) of exomoons around Kepler 16. Our work can be considered as an extension of Quarles et al. (2012), since we consider dynamical stability of exomoons for a wide range of inclination angles, and include all currently-confirmed *Kepler* CBP systems. Other theoretical efforts have revealed a number of interesting properties that distinguish CBPs from single-star host systems. For example, Smullen et al. (2016) showed using N-body simulations that the disruption of multi-planet systems tends to result in far more ejections relative to single-host systems, which more commonly lose their planets due to collisions upon becoming dynamically unstable. Typically, numerical simulations suggest of order 80% of outcomes correspond to ejections, and only 20% to physical collisions with the primary or secondary (Sutherland & Fabrycky 2016). In this chaotic regime, the distribution of escaper velocities has been well-studied and parameterized in previous works, mostly in the context of scattering of single stars by super-massive black hole binaries (e.g., Quinlan 1996; Sesana et al. 2006).

The structure of this paper is as follows. In Section 2, we briefly describe the initial conditions and the numerical methodology used for the N-body integrations and for determining stability regions. The main results are given in Section 3, in which we show the stability maps for the *Kepler* systems. We discuss our results in Section 4, and we conclude in Section 5.

2 METHODOLOGY

2.1 Initial conditions

Our systems consist of a stellar binary (masses M_1 and M_2; semimajor axis a_{bin}) orbited by a CBP (mass M_{p}; semimajor axis a_{p}). In turn, the CBP is orbited by a moon (mass M_{m}; semimajor axis a_{m}). A schematic representation (not to scale) in a mobile diagram of the system (Evans 1968) is given in Fig. 1.

We take the binary and planetary parameters for the currently-known *Kepler* systems from various sources. The adopted orbital parameters are given for convenience and completeness in Table 1. In most cases, the orbital angles are defined with respect to the plane of the sky. Note that the binary's longitude of ascending node, Ω_{bin}, is defined to be zero. For several systems, the argument of periapsis of the binary or the planet is not known. In this case, we set the corresponding values to zero. We do not vary the initial mean anomalies of the binary and the planet (both are set to zero), but we do vary the moon's initial mean anomaly (see below).

Kepler 47 harbors at least two CBPs, Kepler 47b and Kepler 47c (Orosz et al. 2012a), and there may be a third CBP, Kepler 47d (Hinse et al. 2015). Here, we do not consider Kepler 47d, which has not yet been confirmed. Also, we treat the two confirmed planets in Kepler 47 as separate cases, i.e., in each case we neglect the gravitational potential of the other CBP. We have checked that this assumption is justified by running simulations with both confirmed planets included, which yielded no significantly different results. Kepler 64, also known as Planet Hunters 1 (PH1), is a quadruple-star system; the binary+CBP system is orbited by a distant stellar binary (a visual binary) at a separation of $\sim$ 1000 AU (Schwamb et al. 2013). In our integrations, we do not include the visual binary given the large separation between the two stellar binaries, and the relative scale of the inner CBP+planet triplet.

For each binary+planet system, we set up a fourth particle, the exomoon (henceforth simply 'moon'), with mass $M_{\mathrm{m}} = q_{\mathrm{m}} M_{\mathrm{p}}$, where q_{m} is either 0.001 or 0.1, initially orbiting around the CBP (for reference, $q_{\mathrm{m}} \simeq 0.012$ for the Earth-Moon system, $q_{\mathrm{m}} \simeq 4.7 \times 10^{-5}$ for Io-Jupiter, and $q_{\mathrm{m}} \simeq 0.12$ for Pluto-Charon). We consider 40 values of the lunar semimajor axis, a_{m}, on an evenly-spaced grid, with the lower and upper values depending on the system; typically, a_{m} ranges between 0.005 and 0.02 AU (see the figures in Section 3.1 for the precise ranges of a_{m} assumed for each system). The initial eccentricity is set to $e_{\mathrm{m}} = 0.01$; we also carried out simulations with higher initial eccentricities, but found no significant dependence of the stability regions on e_{m}.

The lunar argument of periapsis is set to $\omega_{\mathrm{m}} = 0$; the longitude of the ascending node is set to $\Omega_{\mathrm{m}} = \Omega_{\mathrm{p}} + \pi$, such that the mutual inclination between the planet and the moon is

$$\begin{aligned}\cos(i_{\mathrm{pm}}) &= \cos(i_{\mathrm{p}})\cos(i_{\mathrm{m}}) + \sin(i_{\mathrm{p}})\sin(i_{\mathrm{m}})\cos(\Omega_{\mathrm{p}} - \Omega_{\mathrm{m}}) \\ &= \cos(i_{\mathrm{p}} + i_{\mathrm{m}}),\end{aligned} \tag{1}$$

i.e., by construction, the mutual inclination between the planet and the moon is $i_{\mathrm{pm}} = i_{\mathrm{p}} + i_{\mathrm{m}}$. The inclination of the moon is set to $i_{\mathrm{m}} = i_{\mathrm{grid}} - i_{\mathrm{p}}$, where i_{grid} is evenly spaced from 0 to 180° with 40 values. We consider 10 different values of the lunar initial mean anomaly, $\mathcal{M}_{\mathrm{m}}$, evenly spaced between 0 and 2π. In summary, for each *Kepler* system in Table 1, we carry out $40 \times 40 \times 10 = 16,000$ integrations with different a_{m}, i_{pm} and $\mathcal{M}_{\mathrm{m}}$. These sets are repeated for $q_{\mathrm{m}} = 0.001$ and $q_{\mathrm{m}} = 0.1$ (binary case), and for $q_{\mathrm{m}} = 0.001$ and with the stellar binary effectively replaced by a point mass (single case, i.e., the primary stellar mass is replaced by $M_1 + M_2$, and the secondary stellar mass is reduced to $M_2 = 1\,\mathrm{kg}$, essentially a test particle). This implies a total of $10 \times 3 \times 16,000 = 480,000$ simulations for all 10 *Kepler* CBP systems.

2.2 Determining stability regions

For our integrations, we use ABIE, which is a new PYTHON-based code with part of the code written in the C language for optimal performance (Cai et al., in prep.). ABIE includes a number of integration schemes. Here, we use the Gauß-Radau scheme of 15th order (Everhart 1985), with a minimum time-step of 10^{-13}, and a tolerance parameter of $\epsilon = 10^{-8}$. The integrator incorporates a more sophisticated step-size control algorithm proposed by Rein & Spiegel (2015). We only include purely Newtonian dynamics in our integrations. Strong interactions such as tidal effects, tidal disruption, and the quadrupole moment of the stars and planet are considered posteriori by considering the periapsis distances in the simulations, in Section 3.3. We check for collisions of the moon with the planet and stars, taking the collision radii to be the observed physical radii. In reality, the moon is likely tidally disrupted before colliding with the CBP or with the stars. The tidal disruption radius, however, depends on the density of the moon. Here, we choose a more general approach of setting the collision radii equal to the physical radii.

We carry out 4-body integrations of the binary+CBP+moon system for a duration of $t_{\mathrm{end}} = 1000\,P_{\mathrm{p}}$, where P_{p} is the orbital period of the planet around the binary. To investigate whether this integration time is sufficiently long, we show the stability regions below in Section 3 for different integration lengths. The (absolute values of the) relative energy errors in the simulations after $1000\,P_{\mathrm{p}}$ are typically on the order of 10^{-12}, with maxima of $\sim 10^{-10}$.

We determine stability maps using the following approach. For a given integration time t_{end} and a point in the $(a_{\mathrm{m}}, i_{\mathrm{pm}})$ parameter space, we define the orbit as 'stable' if the moon remains bound to the CBP (i.e., $a_{\mathrm{m}} > 0$ and $0 \leq e_{\mathrm{m}} < 1$) at t_{end} for all 10 realizations with different $\mathcal{M}_{\mathrm{m}}$ (green). If none of the 10 realizations of $\mathcal{M}_{\mathrm{m}}$ yield bound orbits to the CBP, then the orbit is flagged as 'unstable' (red). If the orbit remains bound for some, but not all realizations with different $\mathcal{M}_{\mathrm{m}}$, then we consider the orbit to be 'marginally stable' (yellow).

3 RESULTS

3.1 Stability regions

The main results of this paper are the stability maps shown in Figs 2 and 3, for Kepler 16, and the other 9 *Kepler* CBPs, respectively. In these maps, each point in the $(a_{\mathrm{m}}, i_{\mathrm{pm}})$ plane represents 10 simulations with different initial $\mathcal{M}_{\mathrm{m}}$; green filled circles correspond to stable systems, red crosses to unstable systems, and yellow open circles to marginally stable systems (see Section 2.2 for the definition of stable, unstable and marginally stable systems). If a collision of the moon with the stars or the CBP occurred for one or more $\mathcal{M}_{\mathrm{m}}$-realizations, then this is indicated with either the '–' or '⋆' symbols for collisions with the planet and the stars, respectively. We show the frequency for the most common collision type among the mean anomalies, and the color of these symbols encodes this frequency with respect to the 10 realizations of $\mathcal{M}_{\mathrm{m}}$ (yellow to red for 1 to 10). For collisions of the moon with the stars, the large and small '⋆' symbols correspond to collisions with the primary and secondary star, respectively.

In Fig. 2, the three panels in each row correspond to different integration times: 400, 700 and 1000 P_{p}. In the first and third columns, the mass ratio of the moon to the planet is $q_{\mathrm{m}} = M_{\mathrm{m}}/M_{\mathrm{p}} = 0.001$, whereas in the second column, $q_{\mathrm{m}} = 0.1$. The third column corresponds to the single-star case, in which the stellar binary is replaced by a point mass. In Fig. 3, the integration time is $1000\,P_{\mathrm{p}}$, and the mass ratio is $q_{\mathrm{m}} = 0.001$.

Generally, the maps can be characterized with a stable region at small a_{m}, an unstable region at larger a_{m}, and a marginally stable region in between, as can be intuitively expected. There is also a dependence on i_{pm}, the mutual inclination between the orbit of the moon around the planet, and the orbit of the planet around the inner binary — typically, high inclinations near 90° are less stable than low inclinations (near 0° and 180°), and lead to collisions. The larger instability near high inclinations can be ascribed to LK evolution, and this explored in more detail in Section 3.3. Also, retrograde orbits (i_{pm} near 180°) tend to be more stable than prograde orbits (i_{pm} near 0°), in the sense that the marginal stability region extends to a larger range in a_{m} for retrograde orbits compared to prograde orbits. This is consistent with the general notion that retrograde orbits are typically more stable than prograde orbits owing to the higher relative velocities for retrograde orbits. However, we find that the 'binarity' of the stellar binary is also important, especially for retrograde orbits. This is investigated in more detail in Section 3.2.

As expected, the stability regions decrease for longer integration times. However, there is little dependence on the integration time for the values shown, indicating that $1000\,P_{\mathrm{p}}$ is sufficiently long to determine stability in the majority of the parameter space.

In the figures, we show for reference with the vertical blue dashed dotted lines the Hill radius (e.g., Hamilton & Burns 1992; replacing the binary by a point mass), i.e.,

$$r_{\mathrm{H}} = a_{\mathrm{p}}(1 - e_{\mathrm{p}}) \left(\frac{M_{\mathrm{p}}}{3(M_1 + M_2)} \right)^{1/3}. \tag{2}$$

Note that r_{H} does not lie within the range of a_{m} shown in all figures; if the vertical blue dashed dotted line is not visible, then r_{H} is larger than the largest value of a_{m} shown. Although correct within an order of magnitude, the Hill radius only captures the true stability boundary within a factor of a few. This is not very surprising given that the Hill radius strictly only applies to the three-body case (with the binary replaced by a single body), and does not capture the inclination dependence.

3.2 Mean motion resonances

As mentioned above, the Hill radius does not accurately describe the boundary between stable and unstable orbits in the $(a_{\mathrm{m}}, i_{\mathrm{pm}})$ plane. Here, we consider an alternative simple analytic description of the stability boundary using an interpretation based on MMRs. First, we show in the third row of Fig. 2 and in Fig. 4 stability maps for integrations in which the stellar binary was effectively replaced by a point mass. For Kepler 16, the stable regions are significantly larger in the single-star case, especially for retrograde orbits. This shows that the binary tends to destabilize the moon, as is intuitively clear.

MMRs are due to commensurate orbital periods, and they have been studied in detail for single-planetary systems (e.g., Peale 1976; Sessin & Ferraz-Mello 1984; Batygin & Morbidelli 2013; Deck et al. 2013). For small bodies, MMRs are known to be destabilizing (e.g., the Kirkwood gaps in the Asteroid belt, e.g., Wisdom 1983; Henrard & Caranicolas 1990; Murray & Holman 1997, and rings of Saturn, e.g., Goldreich & Tremaine 1978; Borderies et al. 1982). The dynamics of MMRs in quadruple systems in the 2+2 configuration, which applies to our systems, are not well-understood (see Breiter & Vokrouhlický 2018 for a pioneering study which applies to the case of four bodies with comparable masses). In our configuration, we expect MMRs of the stellar binary with the orbit of the moon around the planet to be important. Since the small-body limit applies, we also expect that these MMRs have a destabilizing effect. As shown by the 'binary case' stability maps, the binary indeed has a destabilizing effect, which is active for $a_{\mathrm{m}} < r_{\mathrm{H}}$, until at a certain value of a_{m} orbits are again stable. For $a_{\mathrm{m}} < r_{\mathrm{H}}$, we expect the latter value to be mainly determined by the 1:1 MMR with the stellar binary.

Using Kepler's law, it is straightforward to show that the condition $P_{\mathrm{bin}} = \alpha P_{\mathrm{m}}$, where P_{bin} and P_{m} are the binary and lunar orbital periods, respectively, and α indicates the order of the MMR,

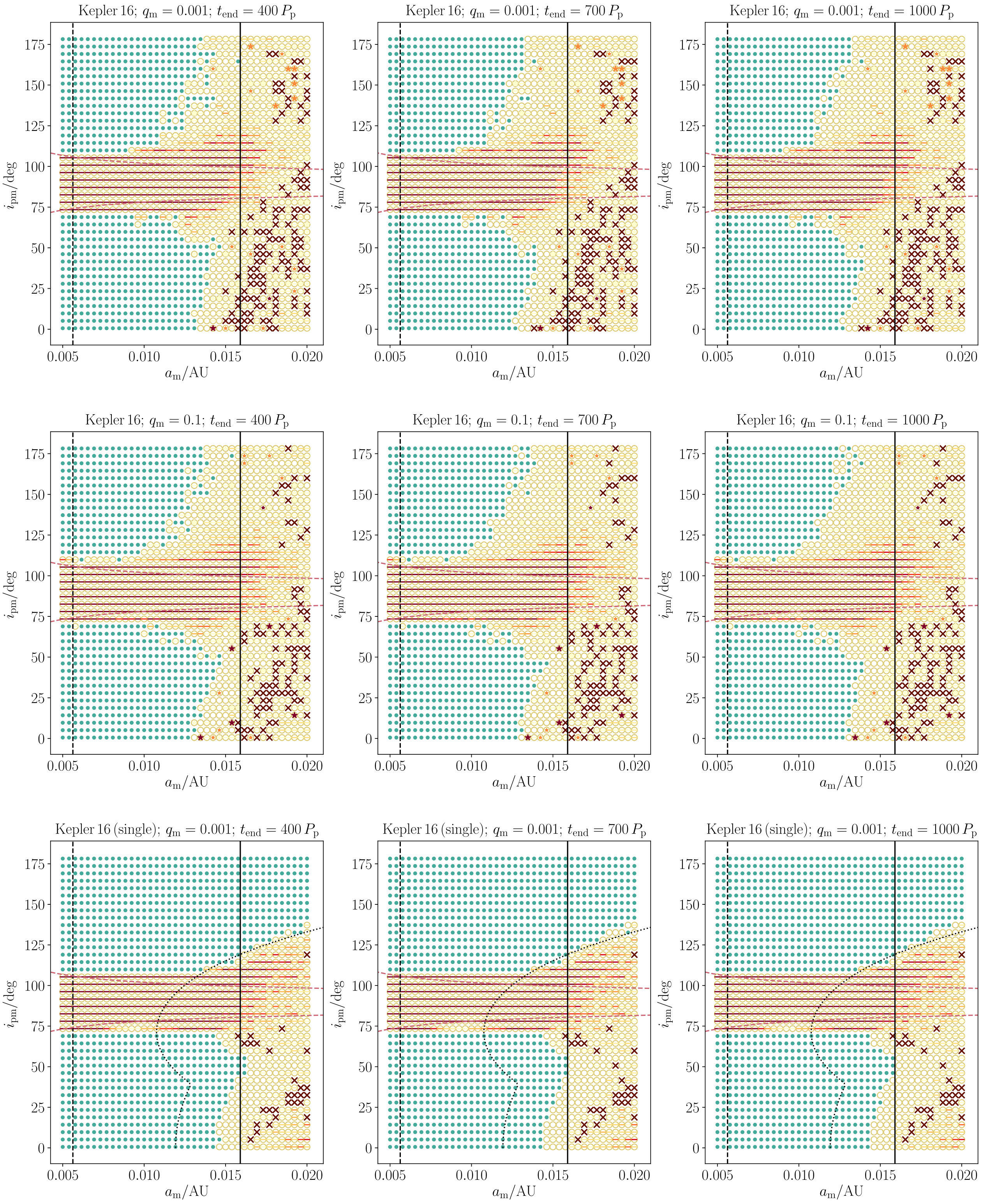

Figure 2. Stability maps for the Kepler 16 system. In each panel, each point represents 10 realizations with different initial lunar mean anomaly, which are used to define stable (green filled circles), completely unstable (red crosses), and marginally stable (yellow open circles) systems. Collisions of the moon with the planet and stars are indicated with '$-$' and '$\star$', respectively, where the color encodes the frequency with respect to the 10 realizations of the initial lunar mean anomaly (yellow to red for 1 to 10). Here, we show the frequency for the most common collision type among the mean anomalies. For collisions of the moon with the stars, the large and small '$\star$' symbols correspond to collisions with the primary and secondary star, respectively. The three panels in each row correspond to different integration times: 400, 700 and 1000 $P_{\rm p}$. In the first and third columns, the mass ratio of the moon to the planet is $q_{\rm m} = M_{\rm m}/M_{\rm p} = 0.001$, whereas in the second column, $q_{\rm m} = 0.1$. The third column corresponds to the single-star case, in which the stellar binary is replaced by a point mass. The vertical black solid lines show the location of the 1:1 MMR of the moon with the binary (equation 3), and the vertical black dashed lines show the locations of the 2:1 MMR. The red dashed lines show the boundary for collisions of the moon with the planet due to LK evolution, computed according to equation (4).

Name	M_1 $\mathrm{M}_\odot$	M_2 $\mathrm{M}_\odot$	M_p M_J	a_bin AU	a_p AU	e_bin	e_p	i_bin deg	i_p deg	Ω_bin deg	Ω_p deg	ω_bin deg	ω_p deg	Ref.
Kepler 16	0.6897	0.20255	0.333	0.22431	0.7048	0.15944	0.0069	90.3401	90.0322	0	0.003	263.464	318.0	1
Kepler 34	1.0479	1.0208	0.22	0.22882	1.0896	0.52087	0.182	89.8584	90.355	0	-1.74	0	0	2
Kepler 35	0.8877	0.8094	0.127	0.17617	0.60347	0.1421	0.042	90.4238	90.76	0	-1.24	0	0	2
Kepler 38	0.949	0.249207	0.00021	0.1469	0.4644	0.1032	0.032	0	0.182	0	0	268.680	0	3
Kepler 47b	1.043	0.362	0.026515	0.0836	0.2956	0.0234	0.035	89.34	89.59	0	0.1	212.3	0	4
Kepler 47c	1.043	0.362	0.072877	0.0836	0.989	0.0234	0.411	89.34	89.826	0	1.06	212.3	0	4
Kepler 64	1.47	0.37	0.531558	0.1769	0.642	0.204	0.1	87.59	90.0	0	0	214.3	105.0	5
Kepler 413	0.820	0.5423	0.21074	0.10148	0.3553	0.0365	0.1181	0	4.073	0	0	279.74	94.6	6
Kepler 453	0.944	0.1951	0.000628	0.18539	0.7903	0.0524	0.0359	90.266	89.4429	0	2.103	263.05	185.1	7
Kepler 1647	1.2207	0.9678	1.51918	0.1276	2.7205	0.1602	0.0581	87.9164	90.0972	0	-2.0393	300.5442	155.0464	8

Table 1. Initial conditions adopted for the *Kepler* CBP systems. See Fig. 1 for a schematic illustration of the definition of the orbital parameters. Here, i, Ω and ω denote inclination, longitude of the ascending node, and argument of periapsis, respectively. The initial mean anomalies for the binary and planetary orbit were set to $\mathcal{M}_\mathrm{bin} = \mathcal{M}_\mathrm{p} = 0$. References: 1 — Doyle et al. (2011); 2 — Welsh et al. (2012); 3 — Orosz et al. (2012b); 4 — Orosz et al. (2012a); 5 — Schwamb et al. (2013); Kostov et al. (2013); 6 — Kostov et al. (2014); 7 — Welsh et al. (2015); 8 — Kostov et al. (2016) .

can be written as

$$a_\mathrm{m,\,MMR} = \alpha^{-2/3}\, a_\mathrm{bin} \left(\frac{M_\mathrm{p}}{M_1 + M_2} \right)^{1/3}. \tag{3}$$

This expression has the same dependence on the masses as the Hill radius (equation 2), but the dependence on $a_\mathrm{p}(1 - e_\mathrm{p})$ is replaced by a_bin. For the 1:1 MMR, $\alpha = 1$; the corresponding values of $a_\mathrm{m,\,MMR}$ are shown in the stability maps with the solid black lines (the 2:1 and 1:2 resonances are shown with the black dashed lines).

As shown in the stability maps, the 1:1 MMR expression captures the boundary between stable and unstable orbits well for most systems, especially for Kepler 35, 38, 47b, 64, and 413, which do not show a strong dependence on i_pm ignoring the region of LK-induced collisions near high inclinations. There are two notable exceptions: for Kepler 47c and Kepler 1647, the stability boundary is significantly larger than $a_\mathrm{m,\,MMR}$, and is more consistent with r_H. In the latter two systems, the CBP semimajor axis is relatively large (more than several times the critical separation for dynamical stability, see, e.g., fig. 1 of Fleming et al. 2018), such that the 'binarity' (i.e., quadrupole moment) of the stellar binary is unimportant. In this case, the 1:1 MMR is expected to be weak, and it should not set the stability boundary. This is supported by a comparison of the maps for Kepler 47c and 1647 in Figs 3 and 4, which reveals that the stability regions for these systems are virtually identical for the single and binary star cases.

3.3 Collisions and strong interactions

As shown in the stability maps, most collisions occur at high inclinations around 90°. In Table 2, we show the number of collisions of the moon with the planet ($N_\mathrm{col,\,p}$), the primary star ($N_\mathrm{col,\,\star 1}$), and the secondary star ($N_\mathrm{col,\,\star 2}$, if applicable). Note that the total number of integrations for each *Kepler* system is 16,000. The majority of the collisions are between the moon with the planet. Collisions of the moon with the stars are rare.

The high-inclination collision boundary has a 'funnel' shape which is symmetric around 90°, and becomes wider at smaller a_m. This can be understood from standard Lidov-Kozai (LK) dynamics (Lidov 1962; Kozai 1962). In particular, in the quadrupole-order test-particle limit and treating the binary as a point mass, the maximum eccentricity for zero initial eccentricity reached is given by

$$e_\mathrm{m,\,max} = \sqrt{1 - \frac{5}{3}\cos^2(i_\mathrm{pm})}. \tag{4}$$

The implied periapsis distance is $r_\mathrm{peri,\,m} = a_\mathrm{m}(1 - e_\mathrm{m,\,max})$ for $\cos^2(i_\mathrm{pm}) < 3/5$, and $r_\mathrm{peri,\,m} = a_\mathrm{m}(1 - e_\mathrm{m})$ (where the initial value is $e_\mathrm{m} = 0.01$) for $\cos^2(i_\mathrm{pm}) \geq 3/5$ (the critical angles for LK oscillations are set by $i_\mathrm{pm} = \arccos(\sqrt{3/5}) \simeq 39.2315°$ and $i_\mathrm{pm} = \pi - \arccos(\sqrt{3/5}) \simeq 140.7680°$). Equating $r_\mathrm{peri,\,m}$ to the planetary radius R_p gives a relation between a_m and i_pm, which is shown in the stability maps with the red dashed lines. These lines generally agree with the simulations at small a_m, at which collisions are driven by LK evolution. At larger a_m, collisions are due to short-term dynamical instabilities rather than secular evolution, and become less dependent on inclination.

The stability maps shown above are based on Newtonian point-mass dynamics, neglecting strong interactions such as tidal effects and tidal disruption. Here, we briefly consider such interactions when the moon passes close to its parent planet (we do not consider strong interactions with the two stars, although, in principle, unstable moons can also experience strong interactions with the binary, see, e.g., Gong & Ji 2018 for the case of scattering-induced tidal capture CBPs).

We evaluate the importance of strong interactions by comparing the periapsis distances of the moon to its parent planet to (multiples of) the radius of the planet. In Fig. 5, we show for Kepler 16 in the $(a_\mathrm{m}, i_\mathrm{pm})$ plane the minimum periapsis distances, $r_\mathrm{peri,\,m}$, recorded in the simulations. Here, we determine $r_\mathrm{peri,\,m} = a_\mathrm{m}(1 - e_\mathrm{m})$ from the minimum value among the systems in the $(a_\mathrm{m}, i_\mathrm{pm})$ plane that are stable (i.e., if the moon remains bound to the planet for all 10 realizations of $\mathcal{M}_\mathrm{m}$); if at least one of the realizations yielded an unbound orbit or a collision, then we set $r_\mathrm{peri,\,m}$ to -0.001 AU, which is indicated in Fig. 5 with the dark blue regions. Note that, due to a finite number of output snapshots, the true closest approach can be missed in some cases. For low inclinations, there is no excitation of e_m, and $r_\mathrm{peri,\,m} = a_\mathrm{m}(1 - e_\mathrm{m,0})$, where $e_\mathrm{m,0}$ is the initial eccentricity. This is manifested in Fig. 5 as a linear relation for small inclinations. For larger inclinations, LK evolution drives high e_m and small $r_\mathrm{peri,\,m}$, and collisions with the planet occur as i_pm approaches 90°.

Also, we show in Fig. 6 a plot of $r_\mathrm{peri,\,m}$ versus i_pm for a slice in a_m, with $a_\mathrm{m} = 0.005$ AU. The latter figure shows that the dependence of $r_\mathrm{peri,\,m}$ on i_pm for $r_\mathrm{peri,\,m} > R_\mathrm{p}$ is well described by the canonical LK relation (equation 4; green dashed line). The red dotted and dashed lines show $r_\mathrm{peri,\,m} = R_\mathrm{p}$ and $r_\mathrm{peri,\,m} = 3\,R_\mathrm{p}$, respectively, where $R_\mathrm{p} = 0.7538\,R_\mathrm{J}$ is the planetary radius (Doyle et al. 2011). Here, we take a factor of 3 to be indicative of the regime where tidal effects are important. Much closer in, tidal disruption is possible, or even direct collision. In the case shown for Kepler 16 and for $a_\mathrm{m} = 0.005$ AU, tidal effects are potentially important for inclinations near 60° and 120°. Direct collision occur for inclinations between ~ 75° and 105°.

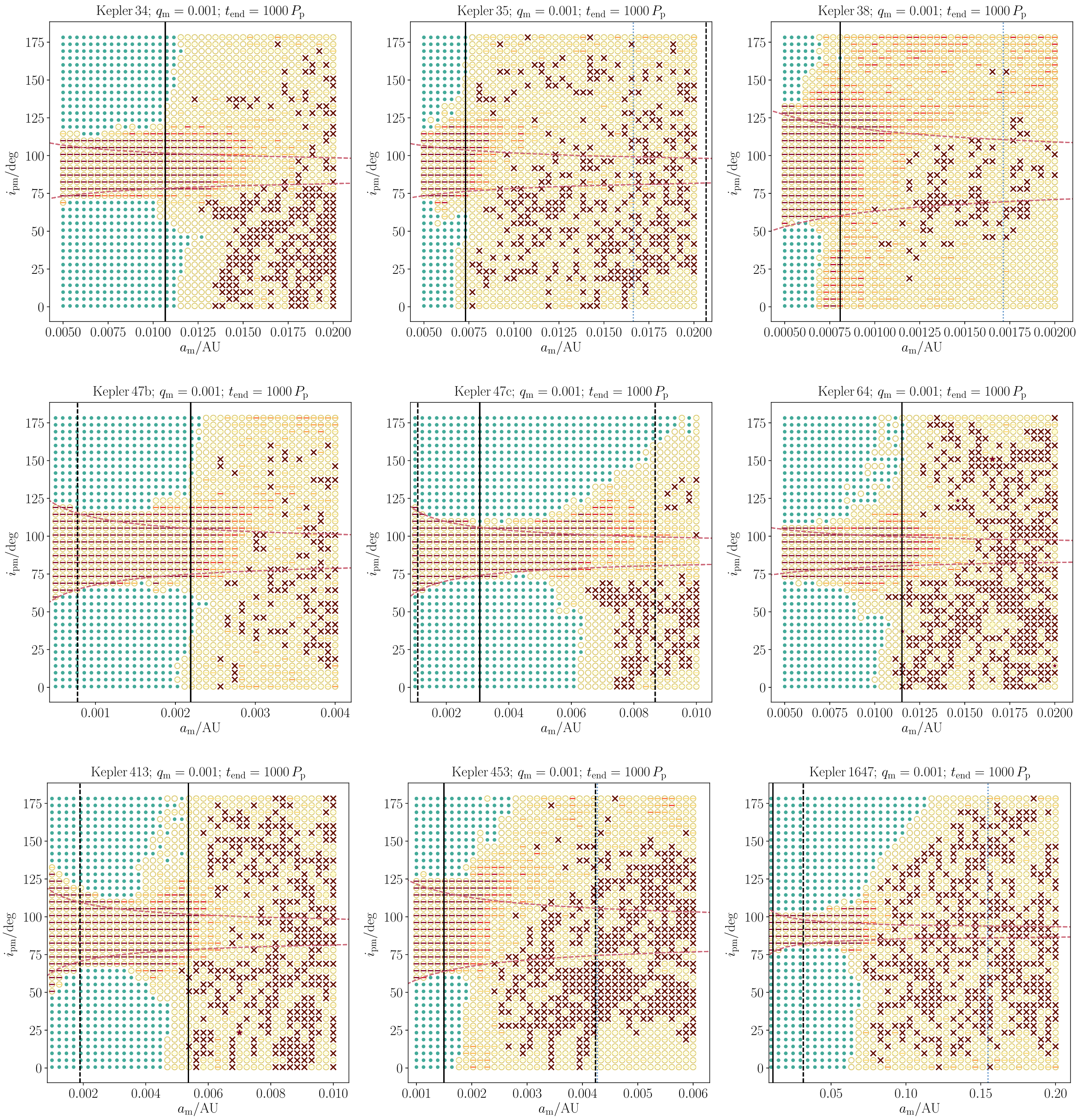

Figure 3. Stability maps for nine *Kepler* CBP systems, similar to Fig. 2. The name of the system is indicated above each panel. In all cases, $q_\mathrm{m} = 0.001$, and the integration time is 1000 P_p. The vertical black solid lines show the location of the 1:1 MMR of the moon with the binary (equation 3); the vertical black dashed lines show the locations of the 2:1 and 1:2 MMRs. The red dashed lines show the boundary for collisions of the moon with the planet due to LK evolution, computed according to equation (4). The vertical blue dashed lines (not visible in all panels) show the Hill radius, equation (2).

3.4 Short-range forces

Our *N*-body integrations include the Newtonian point-mass terms only. Here, we investigate, a posteriori, the importance of short-range forces (SRFs) acting on the planet-moon orbit, in conjunction with LK cycles. Such SRFs can include relativistic precession, and precession due to the quadrupole moment of the planet. In the case of Kepler 16, relativistic precession is completely unimportant since the precession time-scale (on the order of Myr) is much longer than the LK time-scale (on the order of tens of years; see also Table 3).

However, the quadrupole moment of the planet can be important depending on the assumed structure of the planet, and, more importantly, its rotation rate. In Fig. 6, we show with the blue dotted line the periapsis distance $r_\mathrm{peri,\,m}$ according to LK theory with the addition of the quadrupole moment and tidal bulges of the planet (assuming $q_\mathrm{m} = 0.001$). We compute $e_\mathrm{m,\,max}$ by using energy and angular-momentum conservation, with the expressions for the Hamiltonian adopted from Fabrycky & Tremaine (2007). For the

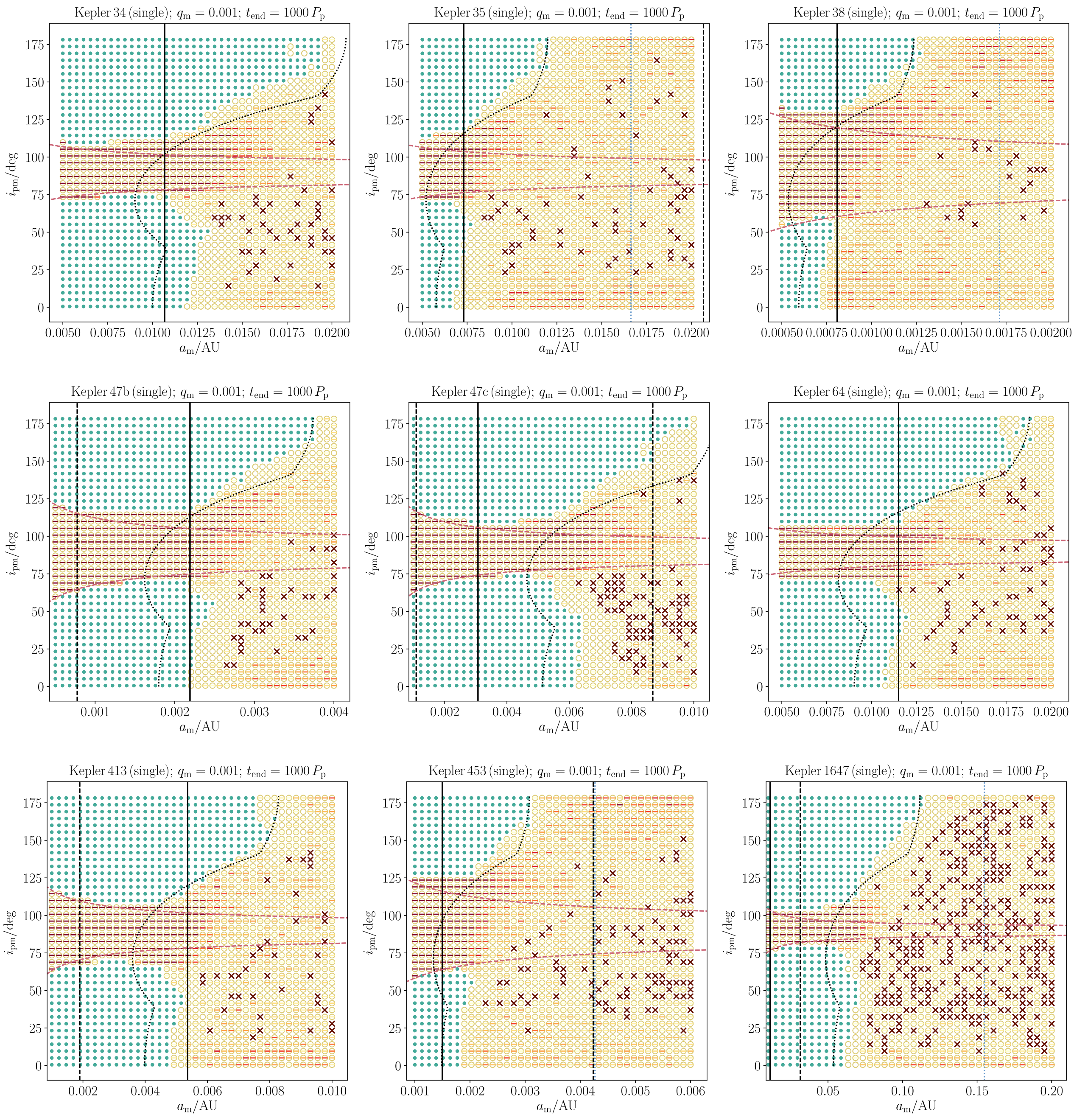

Figure 4. Similar to Fig. 3, now for the single-star case ($q_{\rm m} = 0.001$).

planet, we here assume a spin rotation period of 5 hr (a somewhat extreme case, given that for Kepler 16 the critical rotation period for centrifugal breakup is $2\pi/\sqrt{GM_{\rm p}/R_{\rm p}^3} \simeq 3.4$ hr), and an apsidal motion constant of 0.25. For these values, there is some deviation from the canonical relation equation (4), although, in this case, $r_{\rm peri,\,m}$ is not much affected unless $i_{\rm pm}$ is close to 90°.

To investigate the importance of SRF in all *Kepler* CBP systems, we compute the associated time-scales in Table 3. Approximating the binary as a point mass, the LK time-scale can be estimated as (e.g., Innanen et al. 1997; Kinoshita & Nakai 1999; Antognini 2015)

$$t_{\rm LK} = \frac{P_{\rm p}^2}{P_{\rm m}} \frac{M_{\rm p} + M_{\rm m} + M_{\rm bin}}{M_{\rm bin}} \left(1 - e_{\rm p}^2\right)^{3/2}, \tag{5}$$

where $M_{\rm bin} \equiv M_1 + M_2$. The relativistic time-scale is (e.g., Weinberg 1972)

$$t_{\rm 1PN} = \frac{1}{6} \frac{a_{\rm m} c^2}{G M_{\rm p}} P_{\rm m}, \tag{6}$$

and the tidal bulges (TB) and rotation time-scales are given by (e.g.,

	Binary star ($q_{\rm m}$ = 0.001)			Binary star ($q_{\rm m}$ = 0.1)			Single star ($q_{\rm m}$ = 0.001)	
	$N_{\rm col,\,p}$	$N_{{\rm col},\,\star1}$	$N_{{\rm col},\,\star2}$	$N_{\rm col,\,p}$	$N_{{\rm col},\,\star1}$	$N_{{\rm col},\,\star2}$	$N_{\rm col,\,p}$	$N_{{\rm col},\,\star}$
Kepler 16	3235	106	129	3366	79	110	3193	0
Kepler 34	3120	3	3	3161	1	2	3395	0
Kepler 35	2589	26	22	2695	22	23	4376	0
Kepler 38	5743	0	0	5690	0	0	6059	0
Kepler 47b	4056	0	0	4246	0	0	4205	0
Kepler 47c	3115	0	0	3112	0	0	3281	0
Kepler 64	2442	55	73	2648	55	87	3319	1
Kepler 413	3155	15	10	3246	11	10	3958	0
Kepler 453	3047	0	0	3098	0	0	4727	0
Kepler 1647	1660	0	0	1702	0	0	1977	0

Table 2. Number of collisions of the moon with the planet ($N_{\rm col,\,p}$), the primary star ($N_{{\rm col},\,\star1}$), and the secondary star ($N_{{\rm col},\,\star2}$, if applicable), in the simulations with $q_{\rm m}$ = 0.001 (binary star case), $q_{\rm m}$ = 0.1 (binary star case), and $q_{\rm m}$ = 0.001 (single star case), and for an integration time of 1000 $P_{\rm p}$. The total number of integrations for each *Kepler* system is 16,000.

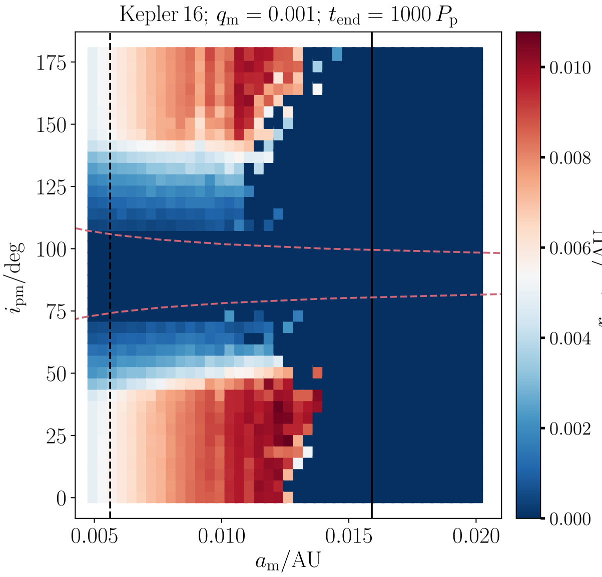

Figure 5. Minimum periapsis distances, $r_{\rm peri,\,m}$, recorded in the simulations in the $(a_{\rm m}, i_{\rm pm})$ plane for Kepler 16. For unbound orbits or collisions, we set $r_{\rm peri,\,m}$ to −0.001 AU, which is indicated with the dark blue regions in the right-hand regions of each panel. The vertical black solid lines show the location of the 1:1 MMR of the moon with the binary (equation 3), and the vertical black dashed line shows the locations of the 2:1 MMR. The red dashed lines show the boundary for collisions of the moon with the planet due to LK evolution, computed according to equation (4).

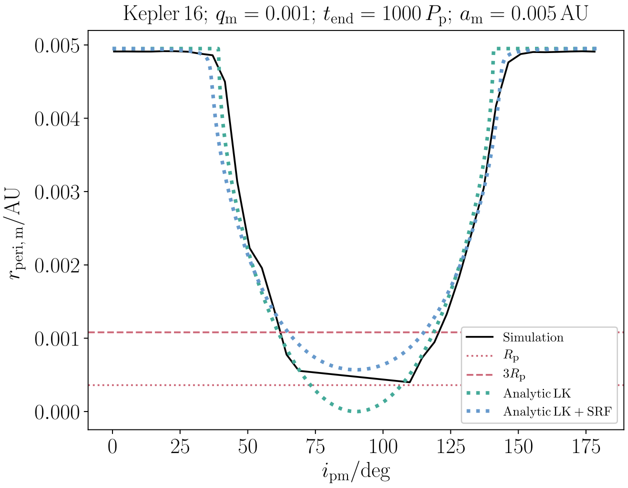

Figure 6. Black solid lines: minimum periapsis distances $r_{\rm peri,\,m}$ for Kepler 16 as in Fig. 5, here for a slice in semimajor axis, i.e., $a_{\rm m}$ = 0.005 AU. Green dotted curve: the analytic LK periapsis distance based on equation (4). Blue dotted curve: analytic LK periapsis distance based on a semianalytic calculation taking into account the quadrupole moment and tidal bulges of the planet (assuming a spin rotation period of 5 hr and an apsidal motion constant of 0.25), and relativistic precession (which is not important). The red dotted and dashed lines show $r_{\rm peri,\,m} = R_{\rm p}$ and $r_{\rm peri,\,m} = 3\,R_{\rm p}$, respectively, where $R_{\rm p} = 0.7538\,R_{\rm J}$ is the planetary radius (Doyle et al. 2011).

Fabrycky & Tremaine 2007)

$$t_{\rm TB}^{-1} = \frac{15}{8} n_{\rm m} \frac{M_{\rm m}}{M_{\rm p}} k_{\rm AM,\,p} \left(\frac{R_{\rm p}}{a_{\rm m}}\right)^5; \tag{7}$$

$$t_{\rm rot}^{-1} = n_{\rm m} \left(1 + \frac{M_{\rm m}}{M_{\rm p}}\right) k_{\rm AM,\,p} \left(\frac{R_{\rm p}}{a_{\rm m}}\right)^5 \left(\frac{\Omega_{\rm p}}{n_{\rm m}}\right)^2, \tag{8}$$

where $n_{\rm m} = 2\pi/P_{\rm m}$ is the lunar mean motion, and $k_{\rm AM,\,p}$ is the planetary apsidal motion constant. In equations (6), (7) and (8), we have set the eccentricity of the lunar orbit to zero. In Table 3, we set $q_{\rm m}$ = 0.001 and $k_{\rm AM,\,p}$ = 0.25, and we assume that the planet is spinning at half its breakup rotation speed, $\Omega_{\rm p,\,crit} = \sqrt{GM_{\rm p}/R_{\rm p}^3}$. The time-scales are shown for two semimajor axes: $a_{\rm m} = a_0$, the smallest semimajor axis considered in the simulations, and $a_{\rm m} = a_1 = a_{\rm m,\,MM}$, the location of the 1:1 MMR with the binary.

As shown in Table 3, relativistic precession and tidal bulges are completely negligible for the *Kepler* CBP systems. Precession due to rotation, i.e., due to the quadrupole moment of the planet, are potentially important at small semimajor axes (in particular for Kepler 47b, 47c, and 453), although it should be taken into account that we assumed a somewhat extreme case of a near-critical rotation speed of the planet.

3.5 Summary plots

We summarize the results of the stability maps by determining the largest stable values of $a_{\rm m}$, $a_{\rm m,\,crit}$, for each system and for a given value of $i_{\rm pm}$, and plotting these values as a function of the masses of

	$t_{\rm LK}$/yr		$t_{\rm 1PN}$/Myr		$t_{\rm TB}$/Myr		$t_{\rm rot}$/yr	
	a_0	a_1	a_0	a_1	a_0	a_1	a_0	a_1
K16	19.8	3.5	5.3	95.0	3.5	6400	5.4	557.5
K34	24.4	7.8	9.8	65.3	4.0	551.9	4.1	165.5
K35	4.0	2.3	22.4	57.8	6.7	78.9	4.0	14.9
K38	3.3	1.6	1061	3520	0.001	0.028	0.001	2.5
K47b	8.3	0.9	0.7	29.8	0.001	10.6	0.1	15.5
K47c	138	25.6	0.9	15.2	0.004	6.5	0.2	12.7
K64	9.0	2.6	2.6	21.0	13.2	2985	32.6	267.1
K413	14.5	1.2	0.2	12.5	0.003	192.0	0.427	59.2
K453	10.6	5.8	1147	3149	0.011	0.15	0.004	6.1
K1647	349	297	3.1	4.0	27.0	53.9	23.8	37.9

Table 3. Short-range precession time-scales for lunar orbits around the *Kepler* CBPs. The time-scales given are the LK, relativistic, TB, and rotation time-scales (see text for details), and are shown for two semimajor axes: $a_{\rm m} = a_0$, the smallest semimajor axis considered in the simulations, and $a_{\rm m} = a_1 = a_{\rm m,MM}$, the location of the 1:1 MMR with the binary. Note that the units for $t_{\rm LK}$ and $t_{\rm rot}$ are yr, and Myr for $t_{\rm 1PN}$ and $t_{\rm TB}$.

the planets and the stars (assuming $q_{\rm m} = 0.001$). In particular, we show in the top panel of Fig. 7 $a_{\rm m,crit}$ normalized to $a_{\rm bin}$ as a function of $M_{\rm p}/M_{\rm bin}$. Different symbols correspond to different inclinations (refer to the legend). Note that high inclinations, near 90°, are excluded since in this case there are no stable orbits in our simulations. Also plotted in the same panel with the solid black line is equation (3), the location of the 1:1 MMR. Most of the data points from the simulations match well with equation (3), again showing that the critical semimajor axis is close to the 1:1 MMR. Two notable exceptions are Kepler 47c and Kepler 1647 (indicated in the figure with arrows), which, as mentioned in Section 3.2, have relatively large planetary semimajor axes, such that the 1:1 MMR is weak and therefore does not set the stability boundary.

Alternatively, one can normalize $a_{\rm m,crit}$ by $a_{\rm p}$. The resulting points from the simulations are shown in the bottom panel of Fig. 7. Again, most of the data are well fit by a power-law function of $M_{\rm p}/M_{\rm bin}$ with a slope of 1/3, although the absolute normalization is different. The black dashed line shows the Hill radius (equation 2), which, as noted above, overestimates the critical $a_{\rm m}$ for stability. However, we can obtain a relation that better describes the data by using the fact that most of the *Kepler* CBPs are close to the limit for stability (i.e., stability of the planet in absence of the moon). In particular,

$$\frac{a_{\rm m}}{a_{\rm p}} = \frac{a_{\rm m}}{a_{\rm bin}}\frac{a_{\rm bin}}{a_{\rm p}} = \left(\frac{M_{\rm p}}{M_{\rm bin}}\right)^{1/3}\frac{a_{\rm bin}}{a_{\rm p}}, \tag{9}$$

where we used equation (3) with $\alpha = 1$ (the 1:1 MMR). Subsequently, we replace $a_{\rm bin}/a_{\rm p}$ by $\langle (a_{\rm p}/a_{\rm bin})_{\rm HW99}\rangle^{-1}$, where $(a_{\rm p}/a_{\rm bin})_{\rm HW99}$ is the critical CBP semimajor axis in units of $a_{\rm bin}$ determined from the analytic fits of Holman & Wiegert (1999), and where the average is taken assuming a thermal eccentricity distribution of $e_{\rm bin}$ and a flat mass ratio distribution (i.e., flat in $q = M_2/M_1$). With these assumptions, we find $\langle (a_{\rm p}/a_{\rm bin})_{\rm HW99}\rangle^{-1} \simeq 0.252267$, such that[1]

$$\frac{a_{\rm m}}{a_{\rm p}} \simeq 0.252267\left(\frac{M_{\rm p}}{M_{\rm bin}}\right)^{1/3}. \tag{10}$$

Equation (10) is shown in the bottom panel of Fig. 7 with the black solid line, and agrees with most of the data from the simulations.

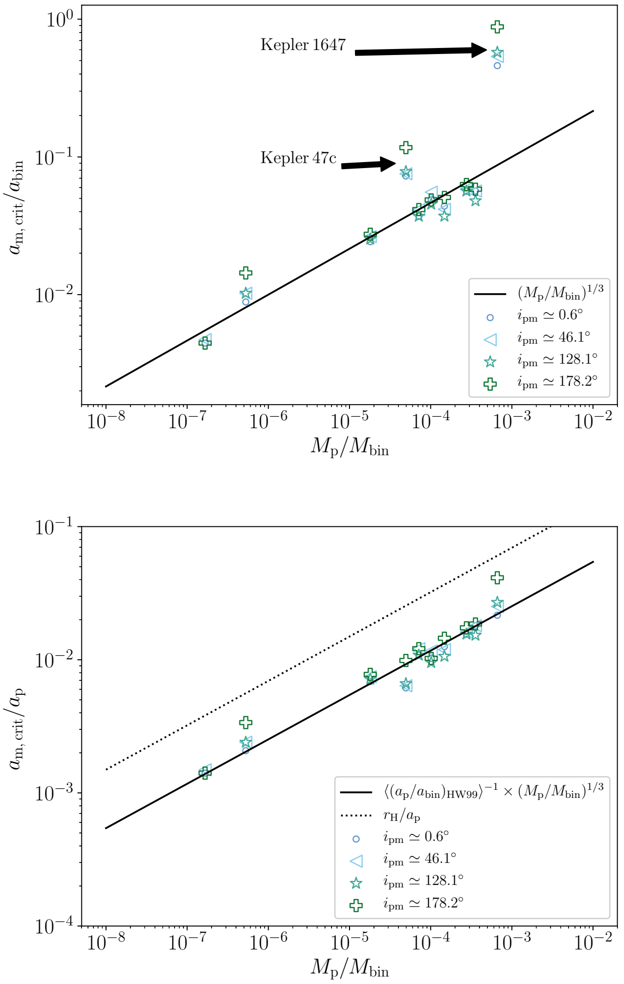

Figure 7. Top panel: largest stable value of $a_{\rm m}$, $a_{\rm m,crit}$, normalized to $a_{\rm bin}$ and plotted as a function of $M_{\rm p}/M_{\rm bin}$, where $M_{\rm bin} = M_1 + M_2$, for each system in the binary case with $q_{\rm m} = 0.001$, and for a given value of $i_{\rm pm}$ (refer to the legend). The solid black line shows equation (3), the location of the 1:1 MMR. Bottom panel: $a_{\rm m,crit}$ normalized to $a_{\rm p}$. The black dotted line shows the Hill radius (equation 2), and the black solid line shows the estimate equation (10) assuming the CBP is close to the critical boundary for stability.

4 DISCUSSION

4.1 Comparison to similar work

In the limit that the binary can be interpreted as a point mass, our results can be compared to Grishin et al. (2017), who considered the stability of inclined hierarchical three-body systems. Grishin et al. (2017) find the following expression for the limiting radii of stability as a function of the mutual inclination, i.e., in our case, $i_{\rm pm}$,

$$r_{\rm c}^{\rm LK}(i_{\rm pm}, e_{\rm m,max}) = f_{\rm fudge}\, 3^{1/3} r_{\rm H}\, g(i_{\rm pm})^{-2/3} f(e_{\rm m,max}), \tag{11}$$

where $g(i_{\rm pm}) = \cos(i_{\rm pm}) + \sqrt{3+\cos^2(i_{\rm pm})}$, and we take the 'corrected' function to be $f(e_{\rm m,max}) = 1/(1+e^2_{\rm m,max}/2)$ with $e_{\rm m,max}$ given by equation (4). The 'fudge factor' $f_{\rm fudge}$ is set to $f_{\rm fudge} = 0.5$, consistent with Grishin et al. (2017).

For the single-star cases, we show equation (11) with the black dotted lines in the third row of Fig. 2 and in Fig. 4 for Kepler 16

---

[1] Alternatively, one could compute $\langle 1/(a_{\rm p}/a_{\rm bin})_{\rm HW99}\rangle \simeq 0.25592$, which gives nearly the same result.

and the other *Kepler* CBP systems, respectively. The absolute locations of the stability boundaries in the simulations do not agree precisely with equation (11). However, the general shapes of the boundaries agree, with the $a_{\rm m}$-boundaries increasing with increasing $i_{\rm pm}$ (i.e., retrograde orbits are more stable in the single-star case), and a 'bulge' near high inclination. Note that equation (11) does not take into account collisions of the moon with the planet, which determine the stability boundaries in the simulations for inclinations near 90°.

4.2 Implications of collisions

As shown above, most of the collisions in our simulations are collisions of the moon with the CBP, and occur at high inclination. However, some of the collisions are between the moon and the stars, and show no strong inclination dependence. Such collisions could enhance the metallicity of the stars, and/or trigger a speed-up of the stellar rotation in the case of a relative massive moon and a low-mass star. Speed-up of stellar rotation has been proposed to occur as a result of planets plunging onto their host star due to high-eccentricity migration (Qureshi et al. 2018).

5 CONCLUSIONS

We investigated the stability of moons around planets in stellar binary systems. In particular, we considered exomoons around the transiting *Kepler* circumbinary planets (CBPs). Such exomoons may be suitable for harboring life, and are potentially detectable in future observations. We carried out numerical N-body simulations and determined regions of stability around the *Kepler* CBPs. Our main conclusions are listed below.

1. We obtained stability maps in the $(a_{\rm m}, i_{\rm pm})$ plane, where $a_{\rm m}$ is the lunar semimajor axis with respect to the CBP, and $i_{\rm pm}$ is the inclination of the orbit of the moon around the planet with respect to the orbit of the planet around the stellar binary. For most of the *Kepler* CBPs and ignoring the dependence on $i_{\rm pm}$, the stability regions are well described by the location of the 1:1 mean motion resonance (MMR) of the binary orbit with the orbit of the moon around the CBP (equation 3). This can be ascribed to a destabilizing effect of the binary compared to the case if the binary were replaced by a single body, and which is borne out by corresponding 3-body integrations. For the two exceptions, Kepler 47b and Kepler 1647, the CBP semimajor axis is relatively large such that the 1:1 MMR is weak, and therefore it does not set the stability boundary.

2. For stable lunar orbits and high inclinations, $i_{\rm pm}$ near 90°, the evolution is dominated by Lidov-Kozai oscillations (Lidov 1962; Kozai 1962). These imply that moons in orbits that are dynamically stable could be brought to close proximity within the CBP, and experience strong interactions such as tidal evolution, tidal disruption, or direct collisions. This suggests that there is a dearth of highly-inclined exomoons around the *Kepler* CBPs, whereas coplanar exomoons are dynamically allowed.

3. Most of the collisions in our simulations are CBP-moon collisions, occurring at high inclination. Collisions with the stars are rare. However, if such collisions do occur, the stars in the binary might be enhanced in metallicity, and/or show an anomalously-high rotation speed.

ACKNOWLEDGEMENTS

This paper is part of the *Moving Planets Around* educational book project, which is supported by Piet Hut, Jun Makino, and the RIKEN Center for Computational Science. ASH gratefully acknowledges support from the Institute for Advanced Study, The Peter Svennilson Membership, and NASA grant NNX14AM24G. This work was partially supported by the Netherlands Research Council NWO (grants #643.200.503, #639.073.803 and #614.061.608) by the Netherlands Research School for Astronomy (NOVA). This research was partially supported by the Interuniversity Attraction Poles Programme (initiated by the Belgian Science Policy Office, IAP P7/08 CHARM) and by the European Union's Horizon 2020 research and innovation programme under grant agreement No 671564 (COMPAT project). MXC acknowledges the support by the Institute for Advanced Study during his visit. Part of this research was carried out at the Jet Propulsion Laboratory, California Institute of Technology, under a contract with the National Aeronautics and Space Administration.

References

Antognini J. M. O., 2015, MNRAS, 452, 3610
Batygin K., Morbidelli A., 2013, A&A, 556, A28
Borderies N., Goldreich P., Tremaine S., 1982, Nature, 299, 209
Breiter S., Vokrouhlický D., 2018, MNRAS, 475, 5215
Cuntz M., 2014, ApJ, 780, 14
Cuntz M., 2015, ApJ, 798, 101
Deck K. M., Payne M., Holman M. J., 2013, ApJ, 774, 129
Dobos V., Heller R., Turner E. L., 2017, A&A, 601, A91
Doyle L. R., et al., 2011, Science, 333, 1602
Dvorak R., 1984, Celestial Mechanics, 34, 369
Evans D. S., 1968, QJRAS, 9, 388
Everhart E., 1985, in International Astronomical Union Colloquium. pp 185–202, doi:10.1017/S0252921100083913
Fabrycky D., Tremaine S., 2007, ApJ, 669, 1298
Fleming D. P., Barnes R., Graham D. E., Luger R., Quinn T. R., 2018, ApJ, 858, 86
Goldreich P., Tremaine S. D., 1978, Icarus, 34, 240
Gong Y.-X., Ji J., 2018, preprint, (`arXiv:1805.05868`)
Grishin E., Perets H. B., Zenati Y., Michaely E., 2017, MNRAS, 466, 276
Haghighipour N., Kaltenegger L., 2013, ApJ, 777, 166
Hamers A. S., Perets H. B., Portegies Zwart S. F., 2016, MNRAS, 455, 3180
Hamilton D. P., Burns J. A., 1992, Icarus, 96, 43
Henrard J., Caranicolas N. D., 1990, Celestial Mechanics and Dynamical Astronomy, 47, 99
Hinse T. C., Haghighipour N., Kostov V. B., Goździewski K., 2015, ApJ, 799, 88
Holman M. J., Wiegert P. A., 1999, AJ, 117, 621
Innanen K. A., Zheng J. Q., Mikkola S., Valtonen M. J., 1997, AJ, 113, 1915
Kane S. R., Hinkel N. R., 2013, ApJ, 762, 7
Kinoshita H., Nakai H., 1999, Celestial Mechanics and Dynamical Astronomy, 75, 125
Kipping D. M., 2009a, MNRAS, 392, 181
Kipping D. M., 2009b, MNRAS, 396, 1797
Kipping D. M., 2014, preprint, (`arXiv:1405.1455`)
Kipping D. M., Bakos G. Á., Buchhave L., Nesvorný D., Schmitt A., 2012, ApJ, 750, 115
Kipping D. M., Hartman J., Buchhave L. A., Schmitt A. R., Bakos G. Á., Nesvorný D., 2013a, ApJ, 770, 101
Kipping D. M., Forgan D., Hartman J., Nesvorný D., Bakos G. Á., Schmitt A., Buchhave L., 2013b, ApJ, 777, 134
Kipping D. M., Nesvorný D., Buchhave L. A., Hartman J., Bakos G. Á., Schmitt A. R., 2014, ApJ, 784, 28

Kostov V. B., McCullough P. R., Hinse T. C., Tsvetanov Z. I., Hébrard G., Díaz R. F., Deleuil M., Valenti J. A., 2013, ApJ, 770, 52
Kostov V. B., et al., 2014, ApJ, 784, 14
Kostov V. B., et al., 2016, ApJ, 827, 86
Kozai Y., 1962, AJ, 67, 591
Lammer H., et al., 2014, Origins of Life and Evolution of the Biosphere, 44, 239
Lidov M. L., 1962, Planet. Space Sci., 9, 719
Martin D. V., 2017, MNRAS, 465, 3235
Martin D. V., Triaud A. H. M. J., 2015, MNRAS, 449, 781
Martin D. V., Mazeh T., Fabrycky D. C., 2015, MNRAS, 453, 3554
Moorman S. Y., Quarles B. L., Wang Z., Cuntz M., 2018, preprint, (`arXiv:1802.06856`)
Muñoz D. J., Lai D., 2015, Proceedings of the National Academy of Science, 112, 9264
Murray N., Holman M., 1997, AJ, 114, 1246
Orosz J. A., et al., 2012a, Science, 337, 1511
Orosz J. A., et al., 2012b, ApJ, 758, 87
Peale S. J., 1976, ARA&A, 14, 215
Quarles B., Musielak Z. E., Cuntz M., 2012, ApJ, 750, 14
Quinlan G. D., 1996, New Astron., 1, 35
Qureshi A., Naoz S., Shkolnik E., 2018, preprint, (`arXiv:1802.08260`)
Rein H., Spiegel D. S., 2015, MNRAS, 446, 1424
Sato S., Wang Z., Cuntz M., 2017, Astronomische Nachrichten, 338, 413
Schwamb M. E., et al., 2013, ApJ, 768, 127
Sesana A., Haardt F., Madau P., 2006, ApJ, 651, 392
Sessin W., Ferraz-Mello S., 1984, Celestial Mechanics, 32, 307
Smullen R. A., Kratter K. M., Shannon A., 2016, MNRAS, 461, 1288
Sutherland A. P., Fabrycky D. C., 2016, ApJ, 818, 6
Wang Z., Cuntz M., 2017, AJ, 154, 157
Weinberg S., 1972, Gravitation and Cosmology: Principles and Applications of the General Theory of Relativity
Welsh W. F., et al., 2012, Nature, 481, 475
Welsh W. F., et al., 2015, ApJ, 809, 26
Wisdom J., 1983, Icarus, 56, 51
Zuluaga J. I., Mason P. A., Cuartas-Restrepo P. A., 2016, ApJ, 818, 160